



Moving boundary models for the growth of crystalline deposits from undetected leakages of industrial process liquors

Michael Dawson^{a,*}, Duncan Borman^b, Robert B. Hammond^a, Daniel Lesnic^c, Dominic Rhodes^d

^a School of Process, Environmental and Materials Engineering, University of Leeds, Leeds LS2 9JT, United Kingdom

^b School of Civil Engineering, University of Leeds, Leeds LS2 9JT, United Kingdom

^c School of Mathematics, University of Leeds, Leeds LS2 9JT, United Kingdom

^d National Nuclear Laboratory, Sellafield, Seascale, Cumbria CA20 1PG, United Kingdom

ARTICLE INFO

Article history:

Received 30 April 2014

Received in revised form 18 July 2014

Accepted 19 August 2014

Available online 16 September 2014

Keywords:

Crystallisation

Mass transfer

Moving boundary problem

Nuclear safety

Computational fluid dynamics

ABSTRACT

In this study, a computational model which simulates the growth of crystalline deposits from dripping salt solution is developed and validated. This problem is of interest to the nuclear industry where the morphology of deposited material impacts on its associated criticality risk. An existing model for simulating geological-stalagmite formations is adapted to the case of dripping salt-solutions which form thin films of fluid that precipitate out over time, forming accumulations. The implementation of a CFD Volume-of-Fluid multiphase model is developed such that the fluid-flow is coupled to the crystallisation kinetics and a moving-boundary model is used for describing the size and shape of growing crystalline deposits. The fluid-flow and forming accumulation are fully coupled, with the model able to account for solute diffusion and solvent evaporation. Results are in good agreement with experimental data for surrogate salt-solutions. Numerical results are presented to assess the sensitivity to process and environmental parameters.

© 2014 The Authors. Published by Elsevier Ltd. This is an open access article under the CC BY license (<http://creativecommons.org/licenses/by/3.0/>).

1. Introduction

Modelling the growth of crystalline deposits plays an important role in a wide range of chemical process driven industries. Applications of computational mass deposition models are diverse; being applied for production and optimisation purposes, to inform process safety and maintenance, and the simulation of formation growth occurring in nature. Computational mass deposition models can relate to the simulation of a variety of physical processes, however here we are specifically interested in the transfer of mass which is contained within a fluid which then deposits on a solid surface. This could be due to either crystallisation or another mass transfer mechanism. Whilst there are some key physical differences between crystal deposition and other mass transfer mechanisms,

the techniques that are used to model them are often similar. Mass deposition models are inherently difficult to solve as it is important that multiple effects are coupled in an accurate and robust manner. The fluid dynamics of the solution flow, crystallisation kinetics and fluid interaction with depositing solids typically need to be considered. For example, in very thin films topological changes from deposited mass can often have a large impact on the flow as the fluid is required to move over or around the body.

A large area of research when modelling crystallisation and mass transfer relates to maintenance, optimisation and future design of equipment (Heath and Livk, 2006; Al-Rashed et al., 2013; Weber et al., 2013). A significant portion of this research relates to capturing fouling phenomena within industrial equipment (Radu et al., 2014; Jun and Puri, 2005). In these situations mass transfer occurs and deposits are formed in pipes or on walls of the equipment. These deposits can affect both the local fluid properties, such as the pressure and velocity, and the heat transfer to and from the equipment walls, as shown by Mayer et al. (2013) when investigating deposition in pipe flows.

The previous works demonstrate the coupling of mass transfer and fluid flow models, they do not specifically concern crystallisation, and do not incorporate crystal growth kinetics within the

Abbreviations: NNL, National Nuclear Laboratory; CFD, computational fluid dynamics; PUREX, plutonium uranium redox extraction; VOF, volume of fluid; UDF, user defined function.

* Corresponding author. Tel.: +44 01133432354.

E-mail addresses: pm09mcd@leeds.ac.uk, MikeC.Dawson@gmail.com (M. Dawson).

<http://dx.doi.org/10.1016/j.compchemeng.2014.08.011>

0098-1354/© 2014 The Authors. Published by Elsevier Ltd. This is an open access article under the CC BY license (<http://creativecommons.org/licenses/by/3.0/>).

Nomenclature

α	volume fraction
Δl	length of linear element (m)
μ	dynamic viscosity (Pa s^{-1})
ν	kinematic viscosity ($\text{m}^2 \text{s}^{-1}$)
ρ	density of solution (kg m^{-3})
θ	angle of inclination from the horizontal
A_a	surface area of gaseous inlet
A_l	surface area of liquid inlet
B	width of film (m)
c	concentration (mol m^{-3})
D	diffusivity ($\text{m}^2 \text{s}^{-1}$)
E	evaporative flux ($\text{kg m}^{-2} \text{s}^{-1}$)
F	rate of deposition ($\text{mol m}^{-2} \text{s}^{-1}$)
G	growth rate (m s^{-1})
h	film height (m)
K	overall growth coefficient (m s^{-1})
k_d	constant of mass transfer (m s^{-1})
k_r	constant of surface integration (m s^{-1})
M_s	molar mass of substance in solid form (kg mol^{-1})
p	pressure (Pa)
p_{atm}	atmospheric pressure (Pa)
Q	mass flow rate of liquid (kg s^{-1})
Q_a	mass flow rate of air (kg s^{-1})
T	solution temperature in the domain
T_{in}	solution temperature prior to entry into domain
\mathbf{g}	acceleration due to gravity (m s^{-2})
\mathbf{n}	unit normal vector
\mathbf{u}	fluid velocity (m s^{-1})

Subscript

aq	substance in aqueous form
i	index of discrete element i
l	substance is in liquid form
q	phase q
s	substance is in solid form

models. Li et al. (2010) posed the growth of a single crystal as a Stefan-type problem solving a scalar diffusion equation for the solution concentration. Crystal kinetics were applied on the crystal surface, such that the growth was proportional to the solution's supersaturation at the surface. This work allowed the modelling of dendritic formations suspended within a stagnant fluid through a front tracking technique. Chen et al. (2009) posed a similar approach for suspended dendritic growth which solved for advection terms in the fluid equations, enabling to capture the motion of a moving solution. These models assume the crystal remains suspended at a fixed, stationary location within the solution. Studies that include crystal kinetic models, such that the crystals are free to move within solution include Heath and Livk (2006), Falola and Borissova (2012) and Cheng et al. (2012). These authors solve population balance models along with a single phase fluid model. The population balance allows the size distribution of the crystals to be captured throughout an industrial batch reactor, this in turn couples to crystal kinetic models to describe the growth. Whilst allowing the mapping of a nonhomogeneous mixture, the crystals in these materials have no impact on the fluid flow and as such, for thin fluid flow, these models do not account for the topological changes on the flow caused by the deposited crystalline mass.

The work in this study relates to modelling crystallisation deposits found in the nuclear industry. In nuclear reprocessing, a popular method of retrieving reusable fuels from spent solid fuel

is the PUREX cycle. This method involves the dissolution of solid plutonium and uranium fuels in nitric acids. This solution is then transported across the plant where it undergoes varying chemical processes. Further details on the PUREX cycle can be found in Phillips (1999). It has been found that in the event of an undetected equipment malfunction, leaking droplets of process liquor can coalesce to form thin liquid films. Solvent loss through evaporation and cooling of the solution through changes in ambient conditions can cause the liquid films to enter a supersaturated state where by crystalline deposits form. Incidents have occurred where the crystalline deposits covering an area of 1 m^2 and 30 cm high, have been observed, details of which can be found in Burrows et al. (2006) and a report by the Health and Safety Executive (2007). These details are of great importance as it is known that for a deposit of heavy metal, the criticality risk of the solid formation depends on both its size and shape.

The purpose of the work here is to model the crystallisation of thin films of a surrogate salt solution. This aim is to offer insight into the size and shape of crystalline deposits which may occur from sustained droplets of industrial process liquor, arising from a long term undetected equipment or pipe leakage, for varying process and environmental conditions. A surrogate salt solution of sodium nitrate is considered as experiments can be conducted conveniently to validate the model. To the best of the authors knowledge, no previous studies have been carried out in order to model this problem.

The NNL have carried out a series of experiments such that a simulant solution of sodium nitrate was dripped onto inclined steel plates (Fig. 1(a)). Over time the drops of solution crystallise and a crystalline formation builds up on the surface of the plate (Fig. 1(b)). Various process parameters were considered in order to develop an understanding of their impact on the resultant crystalline formation.

The experimental work identified a diverse range of formations for changes in input parameters. Impinging droplets of a saturated simulant solution of sodium nitrate (8 M) formed tower-type formations (Fig. 2(a)). For lower concentration solutions (5 M), ring-like configurations were formed (Fig. 2(b)). The criticality implications of these formations change quite significantly for small changes in experimental parameters.

This study will investigate an appropriate model to describe the growth of the formations, and how varying parameters affect the growth and resultant size and shape. Examining the experimental formations it is clear that the crystal mass deposited is large in comparison to the fluid film depth and has a large impact on the flow field. As such, a single phase approach would not be appropriate. It was noted that when observing the deposition of highly concentration salt solutions, similarities could be drawn between these and underground geological stalagmites, albeit on a much smaller timescale. There are a number of published models for predicting the formation of stalagmites overtime (Romanov et al., 2008; Baker and Bradley, 2010; Short et al., 2005a, 2005b; Kaufmann, 2003; Kaufmann and Dreybrodt, 2004). In this study, we adapt a previous geological stalagmite model, Romanov et al. (2008), for the purpose of modelling tower formations formed from supersaturated salt solution. The model uses moving boundary techniques for capturing the crystal growth with a simple analytical model describing the thin laminar film flow. Results from this model offer insight into the crystal deposition behaviour of highly concentrated salt solution. The model neglects certain important physics. As such, a further model is developed using a coupled moving boundary and CFD technique to account for the fluid flow and crystallisation kinetics. This new framework allows the addition of several previously absent physical effects such as diffusion and evaporation. As evaporation is now included, solutions which are not initially in a supersaturated state can also be considered.



Fig. 1. (a) Plates used in NNL drip trials. (b) Example of crystalline mass build up.



Fig. 2. (a) Tower formation of sodium nitrate. (b) Ring formation of sodium nitrate.

2. Mathematical model

2.1. Geological stalagmite models

The model here is based on the work presented in Romanov et al. (2008). The model assumes that a liquid film is initially formed on an inclined linear surface (when considering the problem addressed within the NNL experiments, we assume that the impinging droplets coalesce to form a smooth continuous film). The profile of the growing stalagmite is described by a moving boundary which is discretised into a series of linear elements. These are assumed to give a suitable approximation to the actual surface provided that the number of elements is sufficiently large. Using this assumption it is possible to derive simple analytic expressions to describe the fluid behaviour, as shown below.

2.1.1. Fluid flow of thin films

Assuming that the liquid film is an incompressible fluid, and that the timescales for the fluid flow are much shorter than those of the crystal growth, we can assume that temporal changes within the fluid flow are negligible. Therefore, for a given interval of time, Δt , the liquid film can be described by the steady, two-dimensional, incompressible flow Navier–Stokes equations,

$$\frac{1}{\rho} \nabla p + (\mathbf{u} \cdot \nabla) \mathbf{u} = \nu \nabla^2 \mathbf{u} + \mathbf{g}, \quad (1)$$

$$\nabla \cdot \mathbf{u} = 0, \quad (2)$$

where p is the pressure, $\mathbf{u} = (u, v)$ is the fluid velocity, ρ is the density, ν is the kinematic viscosity, \mathbf{g} is the acceleration due to gravity, $\mathbf{x} = (x, y)$, and θ is the angle of the surface incline, see Fig. 3.

If the flow is sufficiently thin or sufficiently slow (dimensional analysis gives the requirement that the Reynolds number $Re = U_0 h / \nu \ll L^2 / h^2$, where U_0 is the characteristic speed, L and h are the length in the stream-wise direction and of the film thickness, respectively) the inertia term, $(\mathbf{u} \cdot \nabla) \mathbf{u}$, can be neglected and then

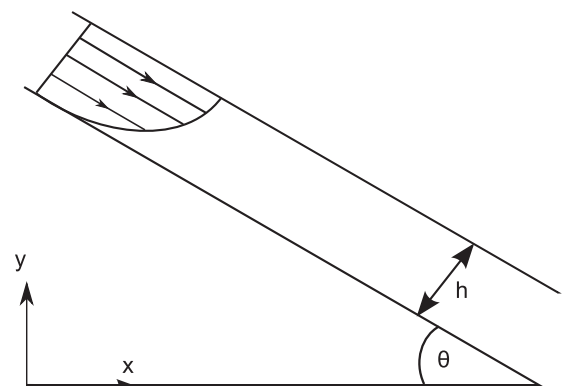


Fig. 3. Flow down an inclined plane.

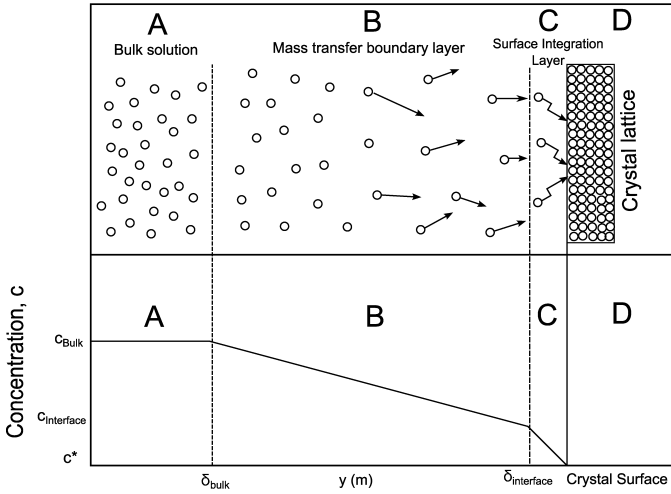


Fig. 4. Two-step crystallisation model.

Eq. (1) can be simplified to become the Stokes equations. This can be then be solved to give the Nusselt film height (Bird et al., 1960),

$$h = \sqrt[3]{\frac{3\mu Q}{\rho^2 g B \sin \theta}} \quad (3)$$

where $\mu = \rho\nu$ is the dynamic viscosity, h is the film height, B is the width of the film and Q is the mass flow rate of liquid.

2.1.2. Two step crystallisation kinetics model

Now that a simple mathematical model has been given to describe the flow field, an advanced model that accounts for the ongoing chemical and crystallisation mechanisms (see Appendix A) needs to be coupled to the flow. The crystallisation model being used within this work is based on a two-step mass transfer/crystallisation model Mullin (2001). This states that the growth rate can be described by two physical processes, occurring at equal rates. The growth rate, G (m s^{-1}), due to diffusion of solute through the film (region B in Fig. 4) can be described by,

$$G(\mathbf{x}, t) = k_d \frac{M_s}{\rho_s} (c(\mathbf{x} + \delta_{\text{bulk}} \mathbf{n}, t) - c(\mathbf{x} + \delta_{\text{interface}} \mathbf{n}, t)) \quad (4)$$

Here, k_d is the coefficient of mass transfer, c is the concentration of solution [mol m^{-3}], $\mathbf{x} = (x, y)$ is the position on the crystal surface. The normal to the crystal surface is given by $\mathbf{n} = \mathbf{n}(\mathbf{x})$. The normal distance between the crystal surface and surface integration layer is given by, $\delta_{\text{interface}}$. Also, δ_{bulk} is the normal distance between the crystal surface and the bulk of the fluid (see Fig. 4). The molecular mass of the solid crystal material in question is given by M_s and the density is given by ρ_s . The growth rate can also be expressed in terms of a surface reaction step, (Region C in Fig. 4). This is the rate in which solute molecules are incorporated into the crystalline lattice, given by,

$$G(\mathbf{x}, t) = k_r \frac{M_s}{\rho_s} (c(\mathbf{x} + \delta_{\text{interface}} \mathbf{n}, t) - c^*)^\eta \quad (5)$$

where k_r is a coefficient of surface integration, $c^* = c^*(T)$ is the concentration at solution saturation for temperature, T , and η is the order of the reaction. Unlike the diffusion term, the surface reaction step is not assumed to be linear, where $0 < \eta \leq 2$.

The authors currently know of no way of analytically or mechanically determining the individual values of k_r and k_d . Whilst the two-step model appears a lot in the literature, it is often difficult to use crystal growth data in order to inversely determine the parameters k_r and k_d , this is mainly due to the inability to accurately

measure the concentration of solute at the surface integration interface, $\delta_{\text{interface}}$. Due to this, experimentalists tend to correlate crystal growth data to the expression,

$$G_e(\mathbf{x}, t) = K \frac{M_s}{\rho_s} (c(\mathbf{x} + \delta_{\text{bulk}} \mathbf{n}, t) - c^*)^\epsilon \quad (6)$$

where K is the overall growth coefficient, ϵ is the overall order of growth and G_e is the observed crystal growth rate. This is often the source of confusion within literature referring to the two-step crystal growth model, as Eq. (6) was initially used purely as an equation to fit crystallisation growth data to a function with accessible input data. This expression allows observed growth rates to be correlated to easily observable parameters such as the concentration in the bulk of the solution. It should be noted that only for specific values of η can an analytical expression for K in terms of k_r and k_d be derived such that $G = G_e$. For example, sodium nitrate and calcium carbonate are known to be linearly dependent on the concentration gradient at the surface integration interface, $\eta = 1$, as demonstrated by Graber et al. (1999) and Oosterhof (1999). Therefore, for this linear order system it can be shown that,

$$K = \frac{k_r k_d}{k_r + k_d} \quad (7)$$

and $\epsilon = 1$. In a similar way analytical expressions can also be obtained for the non-linear example with $\epsilon = 2$.

As the model here solves the fluid system by a steady state approximation (assumed to remain valid over pseudo-timesteps Δt), the continuous growth model described above must be discretised and coupled to the simplified film height given by Eq. (3).

2.1.3. Coupling the fluid flow and crystallisation kinetics

As previously stated, the profile of the formation is approximated by a series of linear elements. We initially divide the initial surface of length L into $N - 1$ elements and consider a general linear element bounded by nodes \mathbf{x}_i^j and \mathbf{x}_{i+1}^j , where $\mathbf{x}_i^j = \mathbf{x}(x_i^j, y_i^j, t_j)$. The initial inclined surface is discretised by,

$$\mathbf{x}_i^0 = \left(\frac{L}{N-1} (i-1) \cos \theta, L \sin \theta \left(1 - \frac{i-1}{N-1} \right), 0 \right), \quad i = 1, \dots, N. \quad (8)$$

The time taken for a parcel of fluid to travel from \mathbf{x}_i to \mathbf{x}_{i+1} is given by τ . Due to the conservation of mass, the amount of solute precipitated into this local area during time τ must equal the amount of solute lost from the surrounding volume of solution. Therefore, given that $\Delta t = t_{j+1} - t_j \gg (N-1)\tau$, for a plate of uniform width B (direction perpendicular to the (x, y) plane) the following mass balance equation is obtained,

$$B \|\mathbf{x}_{i+1}^j - \mathbf{x}_i^j\| F_i^j \tau = B h_i^j \|\mathbf{x}_{i+1}^j - \mathbf{x}_i^j\| (c_i^j - c_{i+1}^j), \quad (9)$$

where $h_i^j = h(\mathbf{x}_i^j)$ (m), $c_i^j = c(\mathbf{x}_i^j, t_j)$ (mol m^{-3}) is the concentration of solute within the solution, and $F_i^j = F(c_i^j)$ ($\text{mol m}^{-2} \text{s}^{-1}$) is the local deposition rate. Here it is assumed that there is no concentration gradient perpendicular to the crystal interface. Given that the deposition rate F_i^j can be written as,

$$F_i^j = G_i^j \frac{\rho_s}{M_s}, \quad (10)$$

where G_i^j is the growth rate at \mathbf{x}_i^j , if $\epsilon = 1$ and $\eta = 1$, Eq. (6) implies

$$F_i^j = K (c_i^j - c^*). \quad (11)$$

Then, from the mass balance Eq. (9), we can obtain the relation,

$$F_{i+1}^j = F_i^j \left(1 - \frac{K\tau}{h_i^j} \right). \quad (12)$$

However, as we want an expression which omits the local film height h_i^j , we use the fact that $h_i^j v_i^j = Q/B$ and $v_i^j = \Delta l_i^j / \tau$, where v_i^j is the average velocity across the element bounded by \mathbf{x}_i^j and \mathbf{x}_{i+1}^j , and Δl_i^j is the length of this element, to obtain the final recurrence relation,

$$F_{i+1}^j = F_i^j \left(1 - \frac{KB\Delta l_i^j}{Q} \right), \quad i = 1, \dots, N-1 \quad (13)$$

and $F_1^j = K(c_1^j - c^*)$.

The nodes are then moved to describe the crystalline growth after a period of Δt by,

$$\mathbf{x}_i^{j+1} = \mathbf{x}_i^j + G_i^j \Delta t \cos \theta_i^j, y_i^j + G_i^j \Delta t \sin \theta_i^j, t_j + \Delta t, \quad i = 1, \dots, N, \\ j = 1, \dots, M, \quad (14)$$

where $M\Delta t$ is the final simulated crystal growth time, G_i^j is determined at each time, t_j , by Eqs. (10) and (13), $\theta_{i+1}^j = \tan^{-1}((y_{i+1}^j - y_i^j)/(x_{i+1}^j - x_i^j))$ and $\theta_1^j = \pi/2$.

In the original stalagmite paper by Romanov et al. (2008), the width of the surface is defined as $B_i(x_i) = 2\pi R_i$, where $R_i := R(x_i)$ denotes the local distance perpendicular to the axis of rotational symmetry. This is because the work assumes the crystalline formation forms an axisymmetric cone-like configuration in which the fluid flows down. This assumption is also imposed in the work here.

2.2. Coupled moving boundary CFD model

The previously described model uses simple analytic expressions in order to capture the height and velocity of the fluid film. The change in solute concentration is described by a bulk mass conservation law across compartments represented by the discrete linear elements. The model neglects key physical processes, such as the diffusion of solute through the film and evaporation of solvent. In order to include these effects, a new coupled CFD model is developed. By using a similar technique to the previous model, crystal growth is described through the use of a moving boundary crystallisation kinetics model. This model is then coupled to a CFD model which describes the fluid flow and the aforementioned, previously neglected physics.

Similarly to the previous model, here we assume that the droplets impact on the surface of an inclined plate. After impact, droplets flow down the incline of the plate, forming a thin liquid film. Due to a temperature drop in the solution and evaporation of the solvent, solubility within the film decreases and crystallisation occurs. Subsequent droplets then interact by flowing over this newly formed crystalline surface. Droplet splashing is neglected within this work as it is assumed the majority of the liquid lands close to the point of impact. As such, the mass flow of the droplets is averaged through time and the liquid enters through an inlet perpendicular to the plate at a constant rate.

2.2.1. Fluid and mass transport

The problem consists of modelling a thin liquid flow, whilst Eqs. (1) and (2) can be used to describe the motion within a single fluid, a multiphase numerical scheme is now required. This will allow both the liquid film, the gaseous phase and the interface between them to be modelled. Additionally, the liquids interaction with any subsequent solid deposition will also be captured.

There are currently many numerical models designed for capturing the flow of multiple fluids. Here we use the volume of fluid (VOF) method which is specifically designed for the modelling of immiscible fluids and capturing the interface between the two. The modelling of thin film flow is a common problem in which the VOF model has been used (Cui et al., 2012; Hirt and Nichols, 1981; Haroun et al., 2010). It is particularly important that we capture the flow and interface accurately, as the velocity and thickness of the liquid film are likely to have a direct impact on the rate and location of crystallisation. This behaviour is verified in Section A.2 of Appendix A.

As with the model presented in Section 2.1, because the crystal growth is a slower process than the fluid flow we assume that within a specified time frame, Δt , the crystal can be assumed stationary and the fluid flow can be approximated by a steady state solution. This is a typical approach when coupling CFD to crystal growth models, as seen in Robey and Maynes (2001). As the total timeframe for crystal growth in these problems tends to span weeks or even months, obtaining a fully transient CFD simulation would generally be considered infeasible. The interface between the liquor solute or salt solution and the gaseous phase is described by the volume fraction equation,

$$\nabla \cdot (\alpha_q \rho_q \mathbf{u}_q) = S_{\alpha_q}, \quad 0 \leq \alpha_q \leq 1, \quad \text{for } q = 2, \dots, n, \quad (15)$$

where ρ_q is the density of the q th phase, S_{α_q} is a the source/sink term relating to the q th phase, $\alpha_q = \alpha_q(\mathbf{x})$ is the volume fraction with respect to the q th phase and n represents the number of phases. The volume fraction equation is not solved for $q = 1$ and is calculated by the fact that in each computational cell,

$$\sum_{q=1}^n \alpha_q = 1. \quad (16)$$

The velocity \mathbf{u}_q satisfies Eqs. (1) and (2). This shared field approach is dependent on the volume fractions of the phases through the properties of ρ and μ , where,

$$\rho = \sum_{q=1}^n \alpha_q \rho_q, \quad (17)$$

such that ρ_q is the fluid density with respect to the q th phase and,

$$\mu = \sum_{q=1}^n \alpha_q \mu_q, \quad (18)$$

where μ_q is the viscosity with respect to the q th phase. In this work the gaseous phase is assumed to be air and the liquid phase is the sodium nitrate solution. Surface tension can be included when using the VOF to model thin film flow (Hu and Kieweg, 2012), however initial studies have shown that this inclusion has minimal impact on the overall crystal growth and is therefore not included in this work.

Transportation of solute within a solution is often described by solving a scalar advection-diffusion equation, as seen in Li et al. (2010), Xu and Meakin (2008), Walker and Sheikholeslami (2006) and Ying et al. (2012). At steady state and when coupled to the VOF method, this equation is given by,

$$\mathbf{u}_q \cdot \nabla(\alpha_2 c) = \nabla \cdot (\alpha_2 D \nabla c), \quad (19)$$

where c is the concentration of sodium nitrate in solution and D is the diffusion coefficient. In this work, $q = 1$ corresponds to the gaseous phase and $q = 2$ corresponds to the liquid solution. Consequently, α_2 is the volume fraction of the liquid phase.

2.2.2. Solvent evaporation

In the physical problem, evaporation plays a key role in the formation of crystalline structures. Evaporation, alongside temperature change, is the dominant driving force for the crystallisation within the NNL drip trials and therefore, a method of modelling such effects should be considered. Evaporative effects are often included within CFD models that predominantly describe either the evaporation of liquid films, see Sultan et al. (2005), Avc et al. (2001) and Ranjan et al. (2011), or the evaporation of sessile droplets, see Sazhin (2006). Applications for such models are extensive ranging from the drying of paper within the textile industry to the de-icing of aircraft systems.

Previous works on modelling evaporative effects when coupled to the VOF model often account for both the loss of mass from the liquid phase, and increase in mass into the gaseous phase. Here, a constant evaporative flux is considered, where flux values will be based on measurements from the NNL drip trial experiments. The mass loss due to evaporation is described by source/sink terms in Eq. (15). Only the loss of mass from the liquid phase is considered here, and therefore the increase in mass to the gaseous phase is ignored, that is, $S_{\alpha_1} = 0$ is not included in Eq. (15).

As the source/sink term in Eq. (15) is a volumetric flux ($\text{kg m}^{-3} \text{s}$), whilst evaporation is a surface reaction ($\text{kg m}^{-2} \text{s}$), this term must be given such that the amount of water extracted is not dependent on the volume of the cells located at the interface. When considering an evaporative flux, $E > 0$ over a surface area A_f , we can state the rate of mass leaving the volume containing that surface must equal,

$$S_{\alpha_2} V_{\text{cell}} = -EA_f, \quad (20)$$

where V_{cell} is the volume of the cell located at the interface. Clearly, this allows one to express the volumetric source, S_{α_2} in terms of the current cell volume and area, to ensure the correct mass of liquid is extracted from the system. The source term in Eq. (20) can then be written as (see Appendix A),

$$S_{\alpha_2} = -E|\nabla\alpha_2|. \quad (21)$$

This term is then included in Eq. (15), which accounts for the loss of mass due to evaporation.

In this work, E is assumed to take a constant value. Despite this, the model can be easily advanced such that E is dependent on water vapour concentrations, temperatures and velocities.

2.2.3. Crystal growth and moving boundary techniques

The approach is based around the two-step crystallisation model presented in Section 2.1.2. This model assumes that crystallisation is based around two physical processes, which are described by Eqs. (4) and (5). By coupling this model to the fluid and mass transport Eqs. (15)–(19) and (21), Eq. (4) is no longer needed as solute diffusion across the mass transfer boundary layer is now accurately captured by the new computational model. As the surface integration layer is generally very small, this is now taken to be at the same position as the crystal surface. Due to this, we can now describe the flux of solute out of solution at the crystal surface by the boundary condition,

$$-D \frac{\partial c(\mathbf{x}, t)}{\partial n} = k_r(c(\mathbf{x}, t) - c^*)^\eta, \quad (22)$$

where \mathbf{n} is the outward unit normal to the boundary and $\eta = 1$ for the sodium nitrate system.

Whilst other works have performed similar calculations using momentum and mass transport equations, such as Robey and Maynes (2001) and Robey (2003) when considering a single phase flow. These works only observed the concentration field at a fixed snapshot in time. The work here now develops this and attempts to model the growth of the crystal through time by the use of a moving

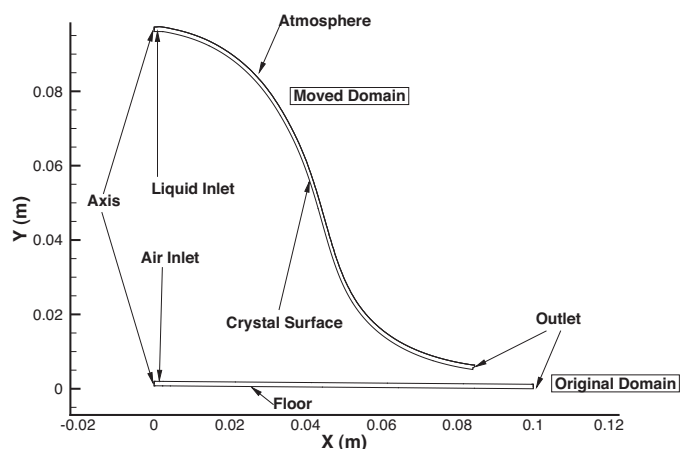


Fig. 5. Plot of the domain before and after successive boundary motions.

boundary technique. This will allow observation of how the fluid and mass fields change with growing crystal topography.

The moving boundary technique which is used in order to describe the crystal growth will be described in detail later, however it should be noted that the crystal growth is dependent on Eq. (22) such that,

$$\Delta \mathbf{S} = -(\Delta t) k_r \frac{M_s}{\rho_s} (c(\mathbf{x}, t) - c^*)^\eta \mathbf{n}, \quad (23)$$

where Δt is the 'pseudo time-step', and $|\Delta \mathbf{S}|$ is the magnitude of the crystal growth at \mathbf{x} in time Δt , where \mathbf{x} is located on the crystalline surface.

3. Computational implementation

3.1. Adapted stalagmite model

The model described by the recurrence relationship in Eq. (13) was implemented in MATLAB. This model initially discretised an inclined plate in which it was assumed that the solution has formed a steady film across. Through the solution of Eq. (13) deposition rates of solid could be calculated down the plate. Once the deposition rates were calculated, the boundary describing the crystalline solids was moved relative to these for a pseudo time-step Δt . This process was carried out iteratively until the final desired time was reached. Reconstruction of the model presented in Romanov et al. (2008) was non-trivial with many details such as the numerical discretisation and time-step size being omitted from the original work.

3.2. Axisymmetric coupled moving boundary CFD model

The model described in Section 2 was implemented and solved using the finite volume CFD software package FLUENT 14.5.

3.2.1. Computational grid

In order for the system of equations to be solved using the finite volume method, a numerical grid or mesh has to be mapped onto the domain. This domain can be seen in Fig. 5. It should be noted that the scales on the figure have been altered for viewing clarity. This model uses a two-dimensional mesh, however rotational symmetry is assumed about the line $x=0$, therefore an axisymmetric three-dimensional situation is in fact considered. When constructing a mesh several things need to be considered. Firstly, when constructing a computational grid, it is desirable to keep the number of cells at a minimum whilst retaining an acceptable solution accuracy. This allows the computational costs to be kept low, such

that increases in cell count have a negligible effect on the solution (mesh independence).

The multiphase VOF model being used to capture the fluid flow, is a diffusive interface model and therefore, there exists a numerical blending between the two regions. Due to this, a refined region of highly refined quadrilateral cells is required such that the interface lies within this region. This is in order to minimise the diffusive flux across the interface.

The last consideration needed when constructing the computational grid, which is specific to the moving boundary approach implemented here, is the robustness of the mesh when deformed using the dynamic meshing. Within the solver procedure, after the boundary nodes relating to the crystal interface have been displaced, the dynamic meshing routine adjusts the other boundaries within the domain in relation to this (in order to keep the volume of the domain from becoming negative or having a very large initial domains size) and also updates the computational grid to fit the new boundary positions. The routine achieves this by assuming that the computational grid is a network of nodes connected via springs, any specified boundary displacement then propagates through this spring network, automatically updating nodal positions throughout the mesh. The dynamic meshing facility has inbuilt remeshing, where if a given cell either exceeds a maximum volume or is less than a minimum volume or becomes too distorted, the model attempts to remesh the region local to this cell. For this facility to work, the mesh must however consist of triangular elements (in two dimensions). This facility is required if the dynamic meshing is to be robust.

As the height of the liquid–gas interface is unknown prior to solving the system of Eqs. (15)–(19) and (21)–(23), an inefficient way of satisfying the first criterion would be to have a highly refined mesh throughout the entire domain. This however would violate the second criterion of keeping the mesh count to a minimum. Therefore, within this work a variable mesh size was used throughout the domain, with the height of the highly refined region being approximated by the analytical expression (3).

As the velocities of the gas phase are specified such that they are very small in comparison to the film flow, they have little impact on the solution and therefore, a coarser mesh can be used throughout this region. In order to satisfy the last criterion when constructing the mesh, a coarse triangular mesh was placed in the region not covered by the refined region. The final mesh which was found to satisfy all the required criteria is shown in Fig. 6. After a comprehensive mesh independence study, it was found that a initial mesh of 40,000 cells was the minimum initial size, such that the resultant formation shape was unchanged for increases in initial cell count.

3.2.2. Boundary conditions

A mass flow boundary condition is placed on both liquid inlets, given by,

$$\mathbf{u} \cdot \mathbf{n} = \frac{Q}{A_l}, \quad (24)$$

where \mathbf{u} is the fluid velocity, \mathbf{n} is the inward normal to the surface, Q is the mass flow rate of liquid and A_l is the area of the liquid inlet. A mass flow rate of,

$$\mathbf{u} \cdot \mathbf{n} = \frac{Q_a}{A_a}, \quad (25)$$

is imposed at the air inlet, where Q_a is the mass flow rate of the air phase and A_a is the area of the gaseous inlet.

The floor and crystal surface have a no-slip boundary condition implemented, where $\mathbf{u} = \mathbf{0}$.

The outlet and atmosphere boundary are classed as a pressure outlets, where a gauge pressure, $p' = p - p_{atm}$ is specified, where p is the absolute pressure and p_{atm} is the atmospheric pressure. Within

Table 1

Boundary condition types for use with the VOF Model in FLUENT CFD.

Boundary	Boundary condition type
Liquid inlet	Mass flow inlet
Air inlet	Mass Flow Inlet
Outlet	Zero gradient pressure outlet
Floor/crystal liquid interface	No slip boundary condition
Atmosphere	Zero gradient pressure outlet

Table 2

Solvers used for the solution of Eqs. (15)–(19) and (21)–(23).

Physics	Solver
Pressure velocity coupling	PISO
Gradient	Least-squares
Pressure	PRESTO
Momentum	First-order upwind
Volume fraction	Modified HRIC

this work we specify $p' = 0$. The boundary conditions for the fluid flow are summarised within Table 1.

The concentration $c = \alpha_2 c_{in}$ is imposed at the inlets and the flux condition (22) is implemented at the floor/crystal–liquid interface using user defined functions (UDF).

The inlet boundaries are placed over a small portion of the boundary adjacent to the rotational axis boundary, the inlets are specified such that they are of equal length to the droplet radius. The domain and boundaries in question can be observed in Fig. 5.

3.2.3. Full solver procedure

Various solvers were used in order to solve the different equations described in the previous section. Discretised versions of Eqs. (1) and (2) were solved within FLUENT using the Pressure Implicit with Split Operator (PISO) algorithm (Issa, 1986) for the pressure-velocity coupling. The PRESTO scheme is used in order to calculate the pressures at the computational cell faces and a least-squares scheme is used to evaluate the gradient terms. A first-order upwind scheme is used to solve the momentum equation. The volume fraction Eq. (15) was solved using the modified High Resolution Interface Capturing (HRIC) scheme (Muzaferija et al., 1999). The scalar transport Eq. (19) was solved using a first-order upwind scheme. A summary of these solvers is given in Table 2.

The solver process was fully automated using the scheme programming environment within FLUENT. This code allows the automatic iteration of the boundary displacement (23), for each steady-state solution of Eqs. (15)–(19), (21) and (22), along with the boundary conditions described in Section 3.2.2. Using a combination of FLUENT scheme code and a UDF, a custom convergence criterion was set. As such, the convergence criterion could be changed such that it was based on surface monitors, such as mass flow rates and surface integrals. Convergence of these monitors showed that Eqs. (15)–(19), (21) and (22) were solved, and the boundary displacement (23) could be carried out. The impact on the size of the pseudo timestep, Δt , in which the boundary was displaced was investigated, and it was found that for an accurate solution $\Delta t \leq 15$ min.

As previously mentioned, the FLUENT dynamic meshing process automatically remeshed regions of poor cell quality, however, it was found that as the problem being modelled here deals with high levels of deformation, this inbuilt remeshing facility was often not capable of handling the imposed deformations whilst keeping an acceptable mesh quality. If the mesh quality was found to be below an acceptable level, the mesh could be remeshed using external meshing software. Fig. 7 shows contours of cell skewness when using the inbuilt facility and after an external remesh. From this

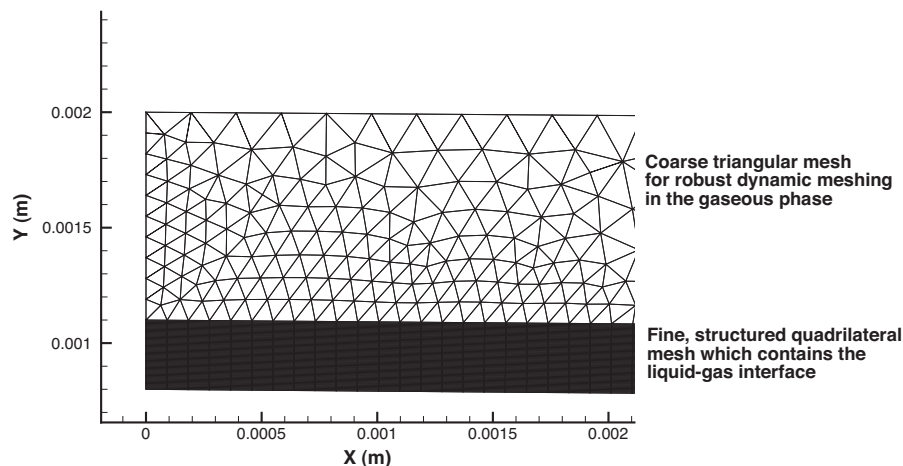


Fig. 6. Example of the combined structured and unstructured mesh. Optimised for use with the VOF and moving boundary model.

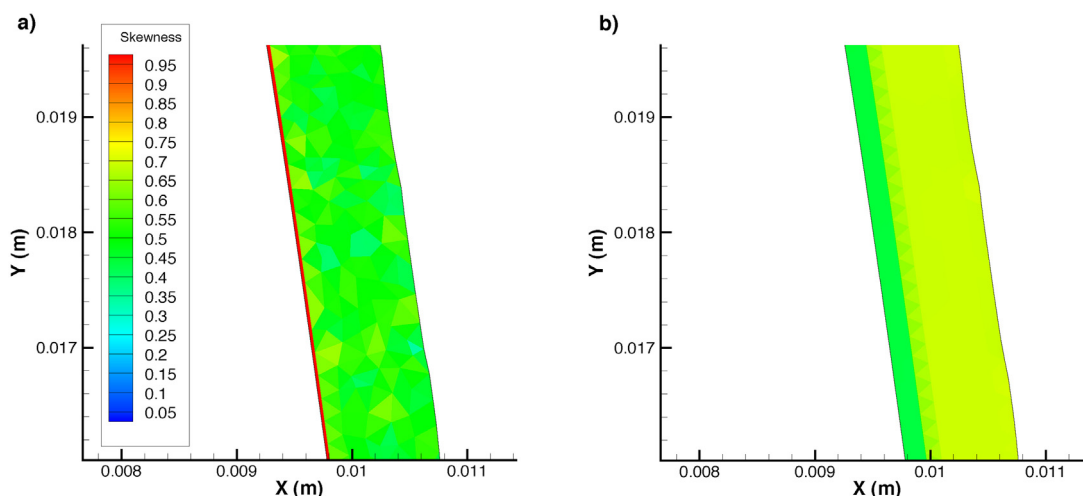


Fig. 7. Comparison of mesh skewness, (a) before and (b) after remesh. (A large value will decrease solution accuracy and can cause divergence in the CFD solver.)

figure it is clear to see that the mesh skewness is much less after the remesh with the external software.

The full solver procedure can be seen within Fig. 8.

4. Results and discussion

4.1. Adapted stalagmite model

Initially, the model for stalagmite growth was reconstructed and verified against the results of Romanov et al. (2008). After this, the parameters were adapted such that the model could be used to capture the salt deposition from impinging droplets of crystallising sodium nitrate salt solution as used in the NNL experiments. Parameters for the modified sodium nitrate case can be found in Table 3 (run 1).

The solubility, c^* [mol m^{-3}], for this material can be expressed as,

$$c^*(T) = 5055.95 + 98.452T, \quad (26)$$

where T is the solution temperature. It is assumed that the temperature of the solution is equal to the ambient room temperature, and remains constant throughout the film. Prior to entry into the system the solution is initially at a higher temperature than the ambient room temperature. Upon entry into the domain the liquid solution experiences a drop in temperature. In order to simplify the

model, we assume that the droplet temperature equilibrates with the ambient room temperature during the free fall phase. As in this work we only consider the film flow after the droplet impact, an isothermal system can be considered. Here we use $\Delta t = 15$ min and the initial length of linear element $\Delta l_i = 3 \times 10^{-4}$ m.

Once the relevant physical and computational parameters have been prescribed, the model was run in order to calculate profiles of an axisymmetric growth. In Fig. 9(a) the growth of these sodium nitrate solutions for an initial concentration, c_{in} , of 8 M can be seen through time. From Fig. 9(a) it can be seen that the tower formations are thinner and grow at a much faster rate to that of the calcium carbonate shown in Romanov et al. (2008). Results are of the same order to those obtained during the sodium nitrate drip trials. The results presented in Fig. 9(a) are axisymmetric approximations of the crystalline structures as they grow through time. Fig. 9(b) shows the three-dimensional representation of the result in Fig. 9(a) for 30 days growth.

As stated in Section 2.1.2, the rate of crystal growth depends on K , the overall growth coefficient, which is a function of k_d and k_r , as shown in Eq. (7). Whilst some literature refers to k_d and k_r as constants, this is technically incorrect as, $k_d = k_d(\mathbf{u}, T)$. The coefficient of mass transfer by diffusion is determined by both the size of the mass transfer boundary layer, δ_{bulk} , which is dependent on the solution velocity, \mathbf{u} and the solute diffusivity, $D = D(T)$. The coefficient of surface integration is dependent on the temperature of

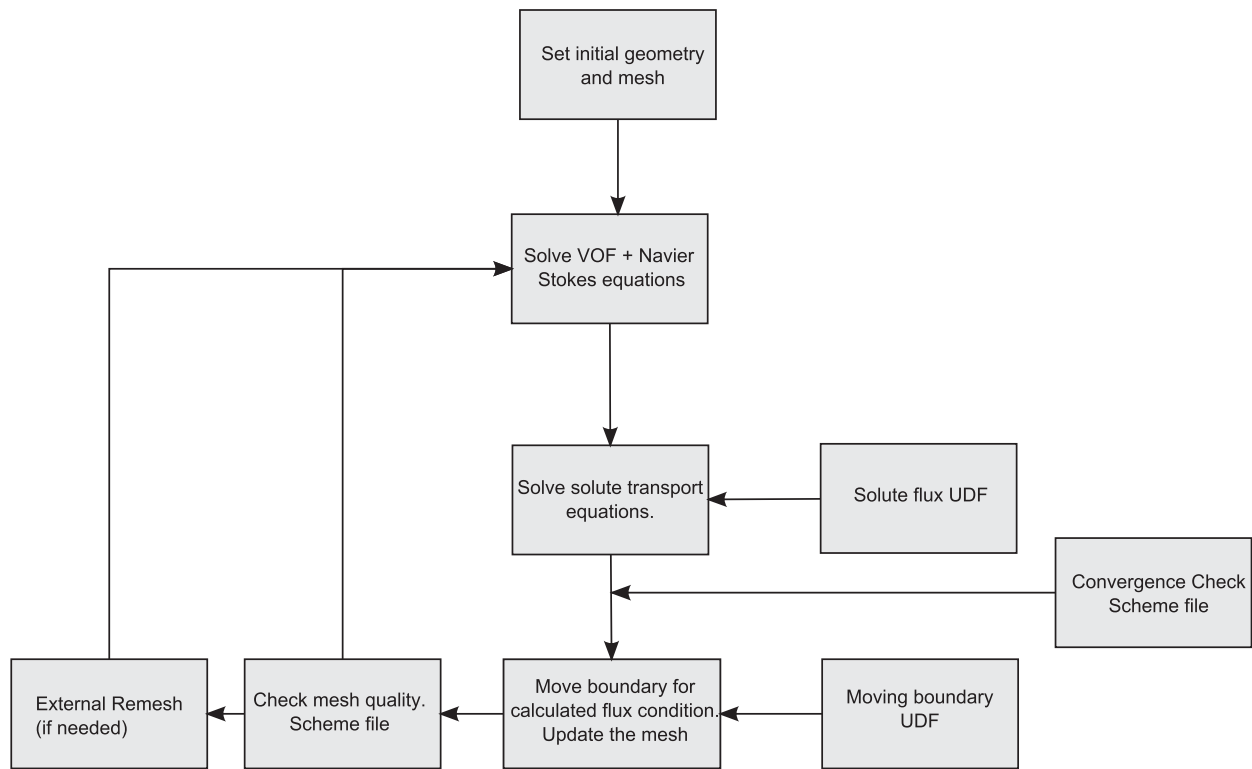


Fig. 8. Flow chart for the solver procedure.

Table 3

Parameters for the computational simulations carried out in this study. Parameters $c_m = 8 \text{ M}$, $\rho_1 = 1.225 \text{ kg m}^{-3}$, $T_{in} = 30 \text{ }^\circ\text{C}$, $\rho_s = 2260 \text{ kg m}^{-3}$ and $M_s = 0.084 \text{ kg mol}^{-1}$ remain fixed for all simulations.

Run	$\rho_2 \text{ (kg m}^{-3}\text{)}$	$\mu \text{ (Pa s)}$	$K \text{ (m s}^{-1}\text{)}$	$Q \text{ (kg}^3 \text{ s}^{-1}\text{)}$	$T \text{ (}^\circ\text{C)}$	$E \text{ (kg m}^{-2} \text{ s}^{-1}\text{)}$	$D \text{ (m}^{-2} \text{ s}^{-1}\text{)}$
1	998.2	0.001	8×10^{-6}	2.89×10^{-5}	27	N/A	N/A
2	998.2	0.001	Varies	2.89×10^{-5}	Varies	N/A	N/A
3	998.2	0.001	8×10^{-6}	Varies	27	N/A	N/A
4	998.2	0.001	8×10^{-6}	2.89×10^{-5}	27	0	1.586×10^{-9}
5	Eq. (27)	Eq. (28)	8×10^{-6}	2.89×10^{-5}	27	10^{-5}	1.586×10^{-9}
6	Eq. (27)	Eq. (28)	8×10^{-6}	Varies	27	10^{-5}	1.586×10^{-9}
7	Eq. (27)	Eq. (28)	8×10^{-6}	2.89×10^{-5}	27	Varies	1.586×10^{-9}
8	Eq. (27)	Eq. (28)	8×10^{-6}	2.89×10^{-5}	27	10^{-5}	Varies

the solution, i.e. $k_r = k_r(T)$. For a particular problem these can often be considered constant, however they may change significantly for other physical scenarios. Various values for K , for sodium nitrate, were calculated in Graber et al. (1999), Oosterhof (1999) and Xu

and Pruess (2009). Despite this, there appears to be no known values for $k_d(\mathbf{u}, T)$ and $k_r = k_r(T)$ for sodium nitrate, therefore results in Fig. 9(a) were generated using an average value of K , taken from these papers. In order to provide a preliminary sensitivity study for

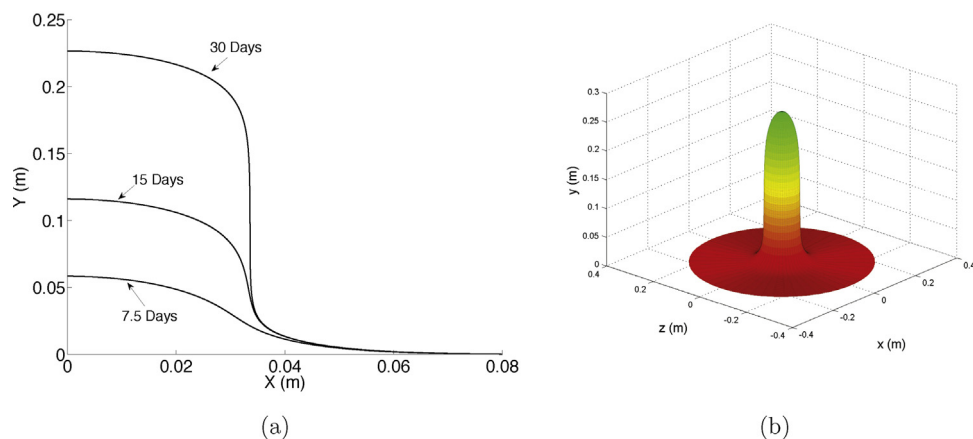


Fig. 9. (a) Axisymmetric plots of the model prediction of the sodium nitrate formation through time. (b) Three-dimensional representation for 30 days growth. Parameters are given in Table 3 (run 1).

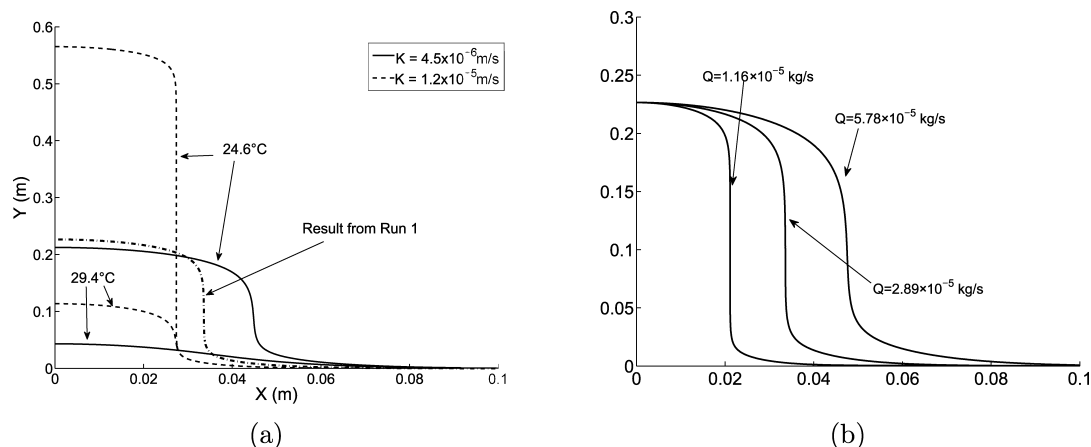


Fig. 10. Axisymmetric plots of the sodium nitrate growth after 30 days growth, for (a) varying temperature, T , and growth constant, K , when $Q = 2.89 \times 10^{-5} \text{ kg s}^{-1}$, $c_{in} = 8 \text{ M}$, $T_{in} = 30^\circ \text{C}$ and (b) for varying mass flow rate, Q , when $K = 8 \times 10^{-6} \text{ m s}^{-1}$, $T = 27^\circ \text{C}$, $c_{in} = 8 \text{ M}$, $T_{in} = 30^\circ \text{C}$.

the parameter K , the model was run for 30 days growth for both the minimum and maximum values of K , observed in Graber et al. (1999), Oosterhof (1999) and Xu and Pruess (2009). In addition to this, a sensitivity study was performed to assess the importance of the ambient temperature, T . The average temperature observed in the NNL trials was 27°C with a standard deviation of 2.4°C . The model was also run with temperatures plus and minus one standard deviation from the mean in order to assess the sensitivity with respect to the temperature. Results from this trial can be seen in Fig. 10(a) for the parameters in Table 3 (run 2).

From this figure it can be seen that as the coefficient K increases, the crystalline formation becomes thinner, but grows vertically at a faster rate. Decreases in ambient temperature (and hence a larger temperature drop from the initial $T_{in} = 30^\circ \text{C}$) causes the tower to grow faster vertically, with no change to the width of the formation. As evaporative rates are dependent on the temperature it is anticipated that a change in temperature would alter the width of the formation if evaporative effects were included.

Changing the mass flow rate, or drip rate of the solution was investigated. Crystalline formations for varying flow rates can be observed in Fig. 10(b) for parameters in Table 3 (run 3). From this figure it can be seen that increasing the mass flow rate increases the width of the formation. As the deposition at the apex F_1 is given by Eq. (10) for $i = 1$, the mass flow rate has no influence on the height of the tower formation.

It can be seen that there is no growth away from the centralised tower formation. However, from Fig. 1(b) it can be clearly seen that in experiments, crystal growth occurs away from the central formation, therefore it can be assumed that additional physics must be considered to reliably retrieve accurate geometrically correct solutions. Currently, the physical processes which are not described by the model include: droplet splashing, evaporation, spatial and temporal variation in the temperature, variable fluid density and viscosity. It is hypothesised that the main cause of crystalline growth in regions away from the centralised formation is due to evaporation.

4.2. Coupled moving boundary CFD model

4.2.1. Model development

The model here was developed in FLUENT CFD. Initial work focused on the development of the mesh, such that the VOF model was solved accurately and the diffusion of the interface was kept to a minimum. A dynamic meshing facility was also developed such that the correct parameters were selected to allow the mesh to undergo large deformations whilst keeping an acceptable level of

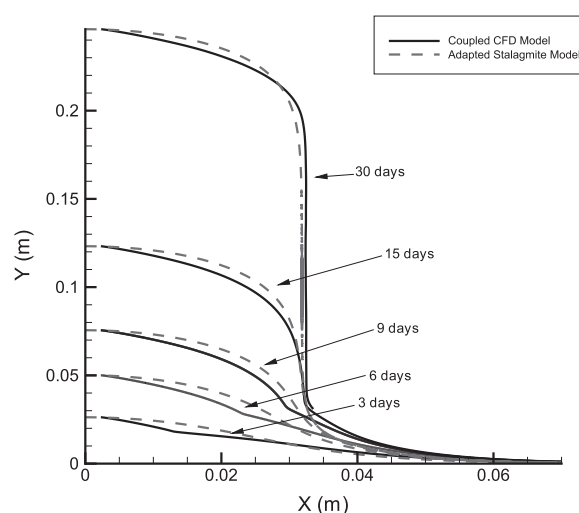


Fig. 11. Axisymmetric formations through time comparing the axisymmetric moving boundary CFD model against the adapted stalagmite model for no evaporation, when $Q = 2.89 \times 10^{-5} \text{ kg s}^{-1}$, $K = 8 \times 10^{-6} \text{ m s}^{-1}$, $c_{in} = 8 \text{ M}$, $T_{in} = 30^\circ \text{C}$.

quality. Initially, UDFs were developed and solver settings were optimised. In order for the results obtained from the model to be physically relevant, a pseudo three dimensional case, such that the solution was axisymmetric about the apex of the formation, was used. The first stage in the development process of the axisymmetric model was to run it with no evaporation. In this study, as the value of the coefficient of surface reaction k_r for sodium nitrate is not available, we consider $k_r \ll k_d$ hence, from Eq. (7), we can assume that $k_r \approx K$. As such, a value of $k_r = 8.9 \times 10^{-6}$ is used throughout the remainder of this study. In addition to this, the air flow during the NNL experiments was intentionally restricted, as such we consider the gas phase not to significantly impact on the liquid film and therefore, impose $Q_a \ll Q$.

Results for a typical case with parameters matching those of Table 3 (run 4) can be seen in Fig. 11. When this prediction is compared to the previous adapted stalagmite model it can be seen that the coupled CFD model predicts a slightly narrower formation than the adapted stalagmite model, in regions close to the apex. In regions further away from the apex of the formation, the coupled CFD model predicts a thicker structure. The maximum heights of the formations are identical due to the constant concentration boundary condition imposed at the inlet. It is hypothesised that the discrepancies in the widths of the formations are due to the

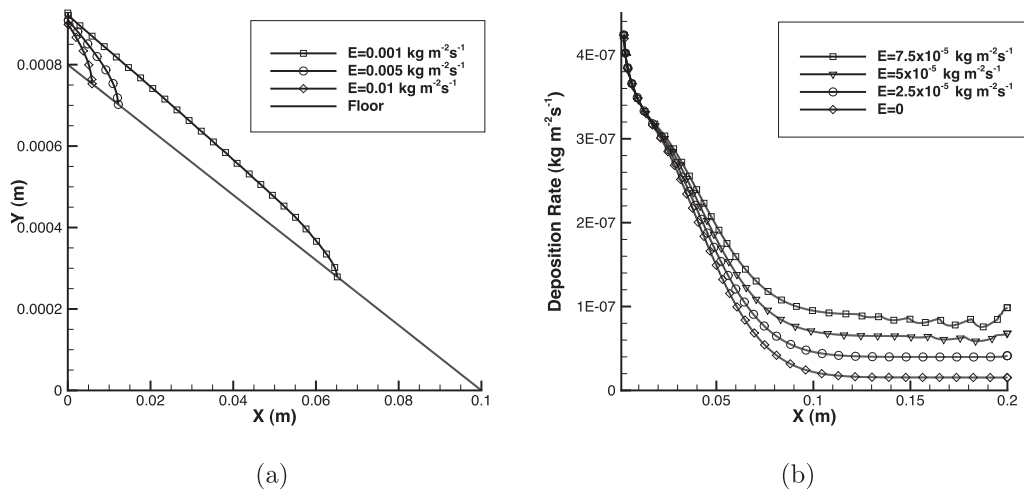


Fig. 12. (a) Two-dimensional plots of a water film for various evaporative fluxes, E . (b) Plot of deposition rates at $t = 0$ for various evaporative fluxes, E , when $K = 8 \times 10^{-6} \text{ m s}^{-1}$, $c_{in} = 8 \text{ M}$, $T_{in} = 30^\circ \text{C}$, $T = 27^\circ \text{C}$.

Table 4

Data for the evaporation of a water film for varying evaporative flux, E .

$E \text{ (kg m}^{-2} \text{ s}^{-1}\text{)}$	Expected interfacial area (m^2)	Calculated interfacial area (m^2)
1×10^{-3}	0.05	0.063
5×10^{-5}	0.01	0.012
1×10^{-2}	0.005	0.0061

inclusion of solute diffusion effects in the coupled CFD model. It is clear that both models, unlike the experimental results, predict no growth away from the central tower formation.

The next stage is the incorporation of an evaporation model. In order to evaluate the basic functionality of the evaporation model, this was applied to a thin liquid film of water for varying constant evaporative fluxes, E . Results for this can be observed in Fig. 12(a). From this figure it can be seen that the film becomes completely evaporated at different points for different evaporative fluxes. As expected, for a larger evaporative flux, the film is completely evaporated quicker and therefore, a smaller interfacial area is observed. For known mass flow into the domain and a given evaporative flux, the expected interfacial area of the film can be calculated (at steady-state). The results for the expected and the computed film areas can be seen in Table 4. From this table it is clear that the evaporation model is working appropriately, however there are small differences between the expected interfacial and computed areas. It is hypothesised that this is due to the inaccuracies involved in calculating the gradient of the volume fraction (from Eq. (21)). Similar inaccuracies are often found when coupling surface tension effects to the VOF model, as seen in Bohacek (2010).

The next stage is to check that the evaporation model functions correctly when coupled to the axisymmetric moving boundary CFD model. Fig. 12(b) shows the deposition rate of crystalline material for varying evaporative fluxes, at $t = 0$ (assuming the film has already spread across the plate). From this figure it can be seen that as the evaporative flux increases, the rate of deposition increases. This effect becomes more pronounced in regions away from the apex of the formation. For large evaporative fluxes an unstable oscillatory solution is observed. It is hypothesised that these instabilities could be due to directly applying the evaporative source to a small interface region. Hardt and Wondra (2008) suggest an interface smearing method such that the evaporative sink is applied over a wider region, however as the evaporative rates experienced in the NNL trials were relatively low, this instability would not be

apparent in the cases present and therefore is not discussed further in the work here.

It should be noted that due to the inclusion of evaporative effects, the model presented here can also be used for the modelling of formations where the solution is not initially in a supersaturated state. In these situations crystallisation would not occur at the point of impact, but rather after the fluid has spread. Once the concentration of the film is increased to a supersaturated state due to evaporation, crystallisation begins. This behaviour leads to a clear region close to the point of impact, a physical example of this can be seen in Fig. 2(b). Whilst the model has capability to do this, the study will focus on analysis of the tower formation growth.

4.2.2. Validation

Following the verification of the axisymmetric model with and without evaporation, the model is next validated against the experimental data available from the NNL drip trials. The density and viscosity in Eqs. (1) and (15) for sodium nitrate are given by (Xu and Pruess, 2009),

$$\rho_2 = \rho_2(c) = a - b(T), \quad (27)$$

and,

$$\mu_2 = \mu_2(c) = 10^{-9} A \sqrt{T + 273.15} e^{B/(T + 273.15 - T_0)}, \quad (28)$$

where $a = 421.37X^2 + 629.7X + 1012.6$, $b = -168.16X^5 + 206.79X^4 - 89.845X^3 + 17.308X^2 - 0.6854X + 0.4789$, $X = cM_s/(cM_s + 1)$ is the mass fraction, $A = 4219.6X^2 + 2995.2X + 991.72$, $B = 300834X^6 + 525458X^5 - 348368X^4 + 106051X^3 + 14531X^2 - 967.34X + 644.92$, $T_0 = 29.088X^2 + 15.881X + 134.68$ and T represents the temperature (in $^\circ \text{C}$).

Using expressions (27) and (28) for a $c = 8 \text{ M}$ solution of sodium nitrate at $T = 27^\circ \text{C}$, we obtain $\rho_2 = 1300 \text{ kg m}^{-3}$ and $\mu_2 = 0.002 \text{ Pa s}$. In addition to this, the diffusivity of sodium nitrate in solution is set to be a constant value of $D = 1.586 \times 10^{-9} \text{ m}^2 \text{ s}^{-1}$, see Yeh and Wills (1970). This value varies slightly with temperature and concentration, however in the work here it is assumed constant.

Including the models for the rheology and diffusivity such that they represent the properties of the liquid solutions used within the experiments, the model can be validated against the experimental work. The experimental temperatures varied through time, such that the mean temperature was $T = 27^\circ \text{C}$ with a standard deviation of 2.4°C . The evaporative flux used in the validation work was assumed constant, with a value of $E = 10^{-5} \text{ kg m}^{-2} \text{ s}^{-1}$, as observed in the experiments. The parameters for the validation case are

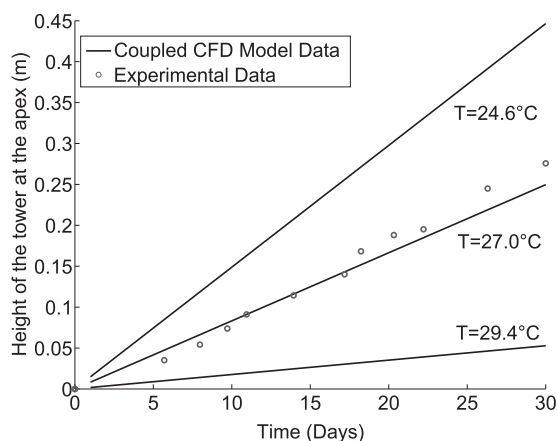


Fig. 13. Height of the formation at its apex through time, when $E = 10^{-5} \text{ kg m}^{-2} \text{ s}^{-1}$, $Q = 2.89 \times 10^{-5} \text{ kg s}^{-1}$, $K = 8 \times 10^{-6} \text{ m s}^{-1}$, $c_{in} = 8 \text{ M}$, $T_{in} = 30^\circ \text{C}$.

summarised in Table 3 (run 5). The model was run using the described validation parameters and the formation heights, at the apex, are presented and compared against experimental results in Fig. 13.

From this figure it can be seen that the model closely resembles the experimental data, for predictions using values close to the mean temperature. The small deviations from this could in part be due to the fluctuations in the temperature. The second metric used when validating the model against experimental data was the tower width. The geological stalagmite models tend to refer to an 'equilibrium radius' such that the width of the formation, tends towards this value. It is noticed however that with the CFD moving boundary models, there is a thickening of the formation close to the crystalline bed. It is unknown whether the experimental data relates to either the equilibrium radius, or the values close to the bed surface. In order to visually clarify the position of the two measurements, these have been highlighted in Fig. 14(a) (run 5). The figure shows a crystalline growth after 3 days, when $E = 0$ and $T = 27^\circ \text{C}$. From looking at Fig. 14(a), the expansion of the formation close to the surface can be observed.

Fig. 14(b) (run 5) shows the experimental widths when compared against the equilibrium radius and formation width at height $H = 0.01 \text{ m}$, produced by the axisymmetric moving boundary CFD model. From Fig. 14(b) it can be seen that the experimental widths measured by the NNL lie in between the equilibrium radius and formation width obtained from the model when run with $E = 10^{-5} \text{ kg m}^{-2} \text{ s}^{-1}$. Unlike the adapted stalagmite model, the equilibrium radius does not remain fixed after a large period of time has passed, instead it continues to grow wider through time. It is hypothesised that this behaviour is due to the evaporation. In order to establish this, the model was run again without evaporation, and the results were plotted on the same figure. From observing the results it is clear to see, that much like the earlier adapted stalagmite model the formation widths approach a constant limiting value.

Both the heights and widths of the formations have been compared and have been shown to be in good agreement with the experimental data. Profiles of the crystalline formations can be compared against the model at various instances through time. Firstly, the model is compared against the formation after 17 days. The results can be observed in Fig. 15(a) (run 5) where it can be seen that the height of the formation is slightly over predicted. The width of the formation is under predicted by the model at the top of the formations, whilst slightly over predicted at lower heights.

The model and experimental results were then compared against a cross-sectional profile of the formation after 30 days

growth. The results for this can be seen in Fig. 15(b) (run 5), where it can be observed that the computational model overpredicts the height at the apex of the formations, but like the previous result the width of the formation is under predicted close to the center of the formation, and moderately overpredicted lower down. However, the model generally predicts the size and shape of these formations well. It is thought that the temperature varied both spatially and temporally during the experimental procedures, however a constant, isothermal system is considered in the model here. It is hypothesised that the slight variations between the model and experimental results could be due to this. Further experiments could be conducted such that additional temperature data is recorded, allowing the aforementioned hypothesis to be investigated further. In addition to this, the splashing effect of the droplets is not considered in the work here as the authors assume it to be negligible, however, further work could also be conducted to confirm this.

4.2.3. Parametric studies

Once the model had shown to give reasonable predictions for the crystalline formations, we now assess how varying parameters, that can typically change within an industrial setting, affect the build up of material through time. In order to assess the effects of altering the mass flow rate, the axisymmetric CFD model was run for varying mass flow rates, Q . Fig. 16(a) shows these results for parameters given in Table 3 (run 6).

From observing the figure it can be seen that as the mass flow rate increases, so does the overall width of the formation. As the mass flow rate decreases, the overall width decreases too. These results are in agreement with the adapted stalagmite model.

A parametric trial was run using a range of evaporative fluxes in order to assess how the formation shape would vary if for example, the environment experienced a change in partial water vapour pressure. Results for 9 days growth when simulated with parameters in Table 3 (run 7), can be seen in Fig. 16(b). From this figure it can be seen that increasing the evaporative flux causes a thickening of the formation away from the apex. These results suggest that in conditions that favour evaporation, the centralised tower formation will not experience much change in overall shape, however there will be a noticeable thickening of the surrounding crystalline bed. This effect could also be expected for higher ambient room temperatures, were the evaporative flux increases and therefore evaporation becomes dominant over the decrease in solution temperature as the driving mechanism for crystallisation. With a increase in temperature the growth rate around the centralised tower formation decreases and in the surrounding regions it increases.

In order for the model to be used when predicting the crystallisation of different materials, it should be run over a range of parameters relating to the material properties. Here we assess both the robustness of the model and the results when trialling varying diffusivity parameters, D . The results, when simulated with parameters given in Table 3 (run 8), can be observed in Fig. 17 where it can be seen that as the diffusivity decreases, the amount of solute deposited close to the apex is reduced. This is due to the solute's ability to flow from the bulk of the solution to the crystal growth site. Due to this, more solute remains within the solution further away from the apex, and as such decreasing D , leads to thicker formations being formed away from the apex. In order to confirm this, the crystal growth from the previous adapted stalagmite model is also plotted on Fig. 17. As the adapted stalagmite model is not limited by diffusion (it has the equivalent of an infinite rate of diffusion in the direction perpendicular to the crystal growth site) it can be seen that this result has the thickest formation close to the apex, and the narrowest formation further away from the apex.

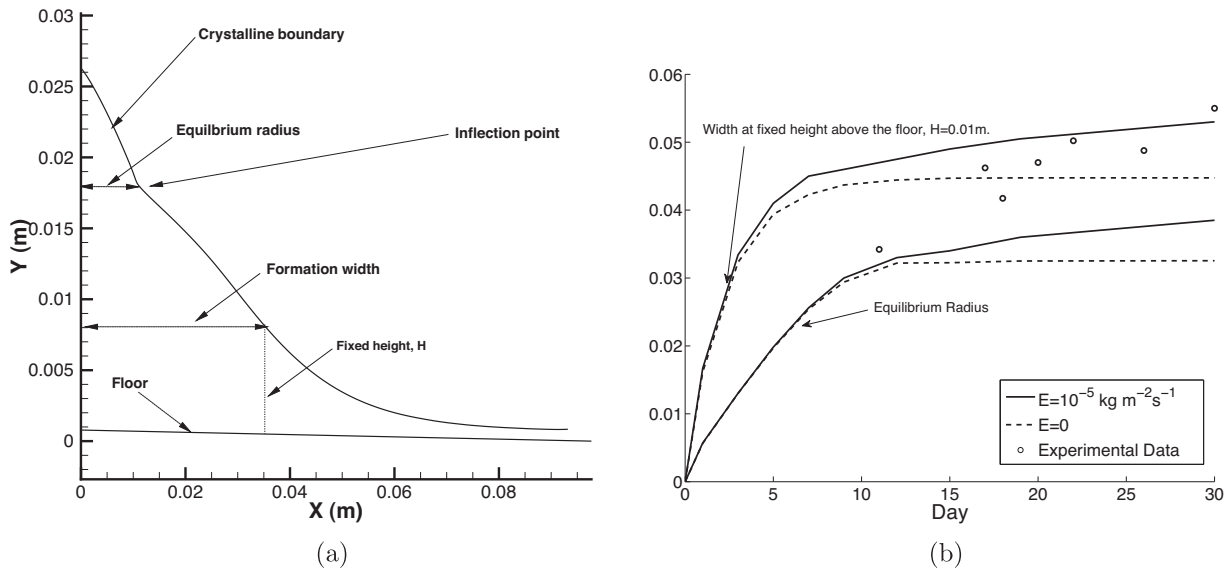


Fig. 14. (a) Plot of tower width measurement locations. (b) Plot of the experimental widths through time compared with the axisymmetric moving boundary CFD model, when $Q=2.89 \times 10^{-5} \text{ kg s}^{-1}$, $K=8 \times 10^{-6} \text{ m s}^{-1}$, $c_{in}=8 \text{ M}$, $T_{in}=30^\circ\text{C}$, $T=27^\circ\text{C}$.

In addition to the diffusivity the effects of varying the solution density are investigated. Although not shown here, a solution of density $\rho_2 = 1560 \text{ kg m}^{-3}$, which is typical of a uranium nitrate solution of concentration 0.3 kg/L in 6 M nitric acid, was also run in the model. Results showed that this increase in density had negligible effect.

Results presented in the parametric study suggest that the final formation is significantly dependent on the material specific crystal growth kinetics, whilst fluid density and material diffusivity have a relatively minor impact. In addition to this, results here suggest that both severity of the leakage (mass flow rate) and environmental parameters, such as room temperature and evaporative rates (temperature, humidity and air velocity) significantly influence the final formation shape.

It should be noted that the work here assumes constant environmental parameters, however through solution of the energy equation, non-isothermal conditions could be specified. These could then be used alongside a temperature dependent

evaporation model. In addition to this, the model can easily account for dissolution of the crystalline material due to increases in solubility (i.e. temperature increase) by providing an appropriate dissolution coefficient in place of k_r (Eqs. (22) and (23)) when $c < c^*(T)$. Coefficients for the dissolution of crystalline materials are determined empirically and are readily available in the literature.

Assuming that the crystallisation behaviour of heavy metals is similar to that of the surrogate solution, the model shows that a formation's size and shape, and hence criticality risk, are strongly linked with both the rates of solution flow and evaporative flux. Therefore, parameters for these should be given careful consideration when using the model for assessing the plant safety.

Parametric tests have also shown that the size and shape of the formation is dependent on the crystal growth kinetics. In order to further validate the model for use in the nuclear industry, experiments could be carried out in order to obtain parameters not currently available in published literature, such as the crystal growth parameters, k_r and η for heavy metal salt solutions.

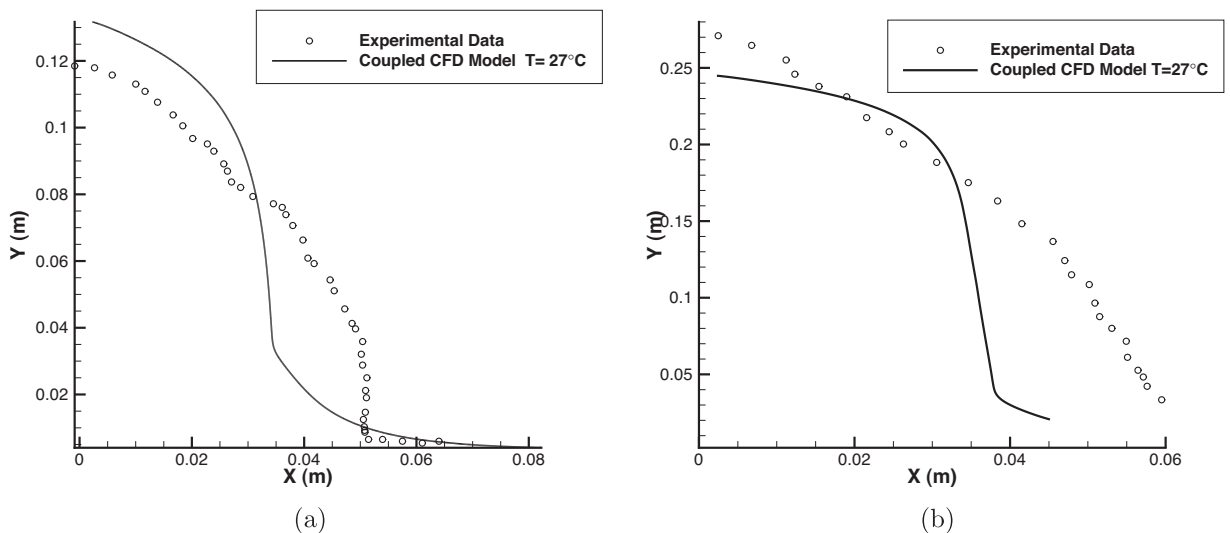


Fig. 15. Comparison of the experimental data and the axisymmetric moving boundary CFD model for the profile of the crystal formation after (a) 17 days growth and (b) 30 days growth, when $Q=2.89 \times 10^{-5} \text{ kg s}^{-1}$, $K=8 \times 10^{-6} \text{ m s}^{-1}$, $c_{in}=8 \text{ M}$, $T_{in}=30^\circ\text{C}$, $T=27^\circ\text{C}$, $E=10^{-5} \text{ kg m}^{-2} \text{ s}^{-1}$.

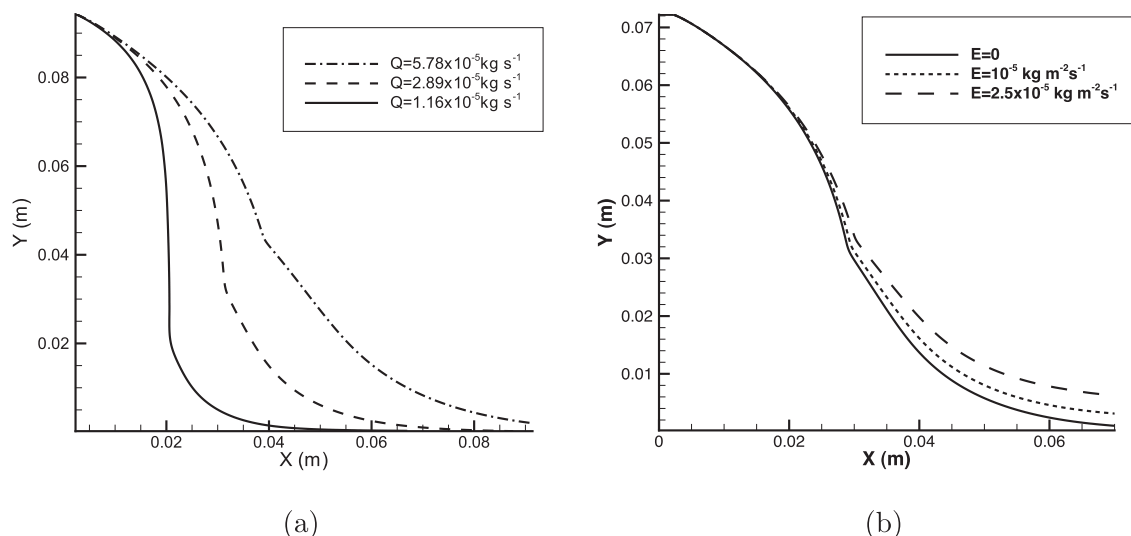


Fig. 16. Axisymmetric plots of the stalagmite through time after (a) 11 days for varying mass flow rates, Q , when $K = 8 \times 10^{-6} \text{ m s}^{-1}$, $c_{in} = 8 \text{ M}$, $T_{in} = 30^\circ \text{C}$, $T = 27^\circ \text{C}$, $E = 0$ and (b) 9 days growth for various E , when $Q = 2.89 \times 10^{-5} \text{ kg s}^{-1}$, $T = 27^\circ \text{C}$, $K = 8 \times 10^{-6} \text{ m s}^{-1}$, $c_{in} = 8 \text{ M}$, $T_{in} = 30^\circ \text{C}$.

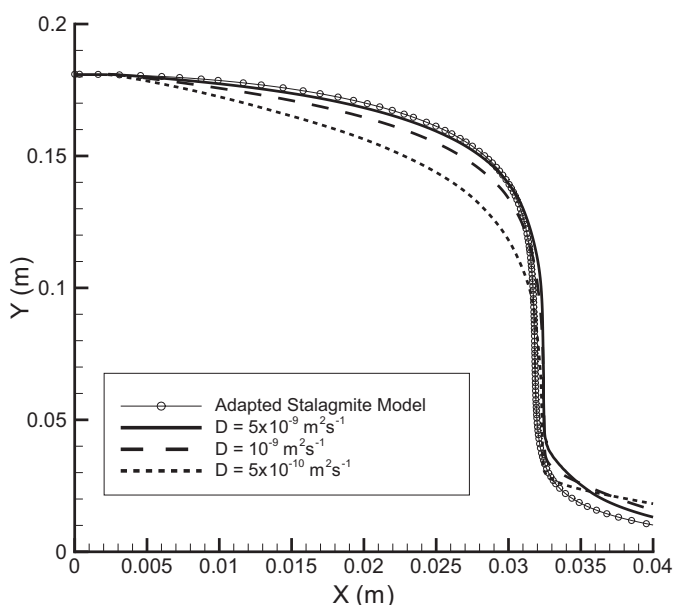


Fig. 17. Axisymmetric plots of the crystalline growth after 22.2 days for varying material diffusivities, D , when $Q = 2.89 \times 10^{-5} \text{ kg s}^{-1}$, $K = 8 \times 10^{-6} \text{ m s}^{-1}$, $c_{in} = 8 \text{ M}$, $T_{in} = 30^\circ \text{C}$, $T = 27^\circ \text{C}$, $E = 10^{-5} \text{ kg m}^{-2} \text{ s}^{-1}$.

5. Conclusions and recommendations

In this study, a geological stalagmite model has been adapted for the purpose of capturing the growth of crystalline formations originating from a dripping salt solution. In the case of heavy metal salt solutions (as found in nuclear waste) it has been previously shown that these have formed films of fluid which precipitate out over time to form accumulations of specific shape and size. Having demonstrated that a simple model can qualitatively simulate some of the key morphology aspects of experimentally observed towers of a surrogate solution (sodium nitrate), a coupled moving boundary CFD crystallisation kinetics model has been developed. The coupled model allows essential physical behaviour associated with the problem to be reliably accounted for (i.e. free-surface film flow, evaporation, diffusion and concentration dependent fluid rheology). The model has been validated using an experimental dataset of controlled growth trials of the surrogate solution where model

predictions are shown to be in good agreement for both the width and height of the formed accumulations through time. The validated model has been used to assess the morphology of formations likely to occur under different process, environment and material conditions.

The main conclusions of the study are:

- A robust model framework has been developed and validated for predicting the shape of crystalline formations formed from dripping salt solution over time.
- Both the solution flow rate and the environmental conditions (affecting the rate of evaporation) have a large impact on the width and overall shape of resultant formations.
- Both the solution temperature and the solutions crystal kinetic constant, K , have a large impact on the width, height and overall shape of the formation.
- The solute diffusivity has a small impact on the shape of the tower formation and the solution density has negligible impact for the considered range of parameters investigated.

The applicability of the model for the simulation of crystalline deposition of heavy metal salts has also been considered. It is recommended that input data for temperatures, liquor flow rates and environmental factors affecting the rate of evaporation should be given close consideration if using the model for criticality safety assessments. It is proposed that further studies are needed to reduce uncertainty in crystalline growth parameters for particular heavy metal solutions. This will provide wider opportunity to apply the modelling approach. Furthermore, it is noted that the model is not restricted to predicting tower formations and the approach has applicability for cases involving temperature related crystallisation and dissolution for non-isothermal systems, where a much wider range of formation morphology are observed to occur. The approach presented in the paper provides a robust, versatile model to be applied for use over a full range of environment, process and material parameters.

Acknowledgments

The authors would like to thank the EPSRC (Industrial CASE grant number: EPH5013551), the National Nuclear Laboratory and Sellafield Ltd. for their continual funding and

support. The comments and suggestions made by the referee are also gratefully acknowledged.

Appendix A.

A.1. Crystallisation mechanisms for both geological and surrogate salt solutions

Crystallisation from salt solution involves free ions within the liquid solution being integrated into a solid crystalline lattice. Whilst the chemical materials and reactions may be different between the stalagmite growth and the crystallisation of process liquors, the fundamental principle is the same. For instance, when considering stalagmite growth modelled in Romanov et al. (2008), CO₂ is absorbed from the atmosphere and surrounding soil, increasing the solubility of the water. This in turn allows the water to dissolve calcium carbonate, obtained from predominantly limestone within the soil, forming calcium bicarbonate (the forward reaction in Eq. (29)),



where *s*, *l* and *aq* represent the molecules in their, solid, liquid and aqueous forms, respectively. The calcium bicarbonate solution then flows down into underground caves, where the CO₂ concentrations are much lower. The change in concentration causes CO₂ to leave the solution, which in turn makes the solubility to decrease within the solute and crystallisation to occur (backward reaction in Eq. (29)). This process is known as CO₂ degassing, and it is the driving mechanism for crystallisation in the case of stalagmite and various other speleothem formations.

When considering the problem addressed within the NNL experiments, inorganic salt solutions are dissolved within solvent and are passed through pipes as part of an industrial process. Here we will consider a simulant reaction between water and sodium nitrate, as shown by,



If a leakage occurs within the pipe, fluid exits and collects on a surface. This solution is now subject to both a temperature change and solvent evaporation. These factors can cause the solubility of the solution to decrease, and crystallisation to occur (backward reaction in Eq. (30)). Therefore, in comparison to the stalagmite case, the driving mechanism in this case is both a decrease in solvent volume and a decrease in temperature, as opposed to the CO₂ degassing mechanism previously described in Eq. (29).

A.2. Crystal growth rates sensitivity to the film velocity and interface height

As mentioned previously in Section 2.2.1, the crystal growth rate is dependent on the film height and velocity. In order to verify this statement, the instantaneous growth rate at *t* = 0 (assuming a fully developed flow) was calculated for a film of height, *h* = 0.001 m and horizontal velocity *u* = 0.0001 m s⁻¹. Film heights and solution velocities were then perturbed in order to assess the changes on the crystal growth rate. As the solution velocity and film height are coupled it was not possible to use the VOF model to isolate and change each variable independently. Therefore, a single phase fluid model was used, such that Eqs. (1) and (2), with boundary conditions imposed such that to mimic a fluid film, were solved. This approach allowed the film height or velocity to be changed, whilst keeping the other fixed in order to monitor their impact on the crystal growth. An example of the fluid film can be seen in Fig. 18. In this figure there is a no slip boundary condition on the floor such that *u* = 0, and a no shear boundary condition on

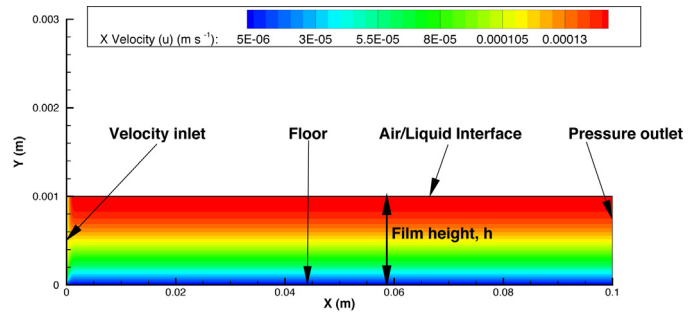


Fig. 18. Example of a liquid film with contours showing the horizontal velocity, *u*.

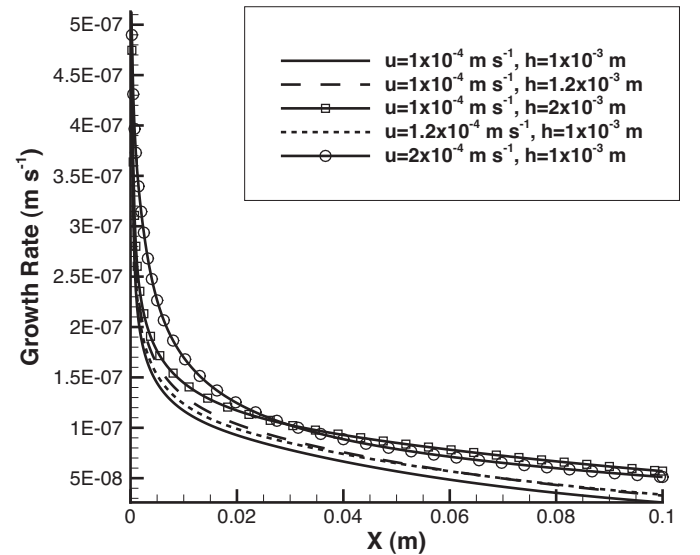


Fig. 19. Plot of the instantaneous crystal growth rates, normal to the surface, for varying film height and velocity, when *K* = 8 × 10⁻⁶ m s⁻¹, *c_{in}* = 8 M, *T_{in}* = 30 °C, *T* = 27 °C.

the air–liquid interface, such that ∂*u*/∂*y* = 0. A constant velocity is imposed across the inlet, and a zero pressure outlet, *p* = 0, is given. Fig. 19 shows the changes in crystal growth rates for various film heights and velocities. From this figure, it is clear to see that both the film height and velocity have a noticeable effect on the growth rate. When observing the crystal growth over timescales of interest in this work, these differences are likely to cause a substantial change in the total deposited mass.

A.3. Derivation of the evaporative source

As the VOF model for free surface is a diffusive model, the lack of a well-defined interface can make it difficult to give a value for the interfacial area, *A_f*. Within this work we employ a technique used in Hardt and Wondra (2008), which also incorporates an evaporative model for use with the VOF model. This states that

$$\int_{\Omega} |\nabla \alpha_2| d\Omega = \int_A dA, \quad (31)$$

where Ω is a volume containing the liquid–gas interface, $|\nabla \alpha_2|$ is the magnitude of the gradient vector of the volume fraction of water, and *A* is the interfacial surface area within the volume Ω . Therefore, for an individual cell, the following holds,

$$|\nabla \alpha_2| V_{cell} = A_f, \quad (32)$$

where *V_{cell}* is the volume of the cell located at the interface and *A_f* is the interfacial area of the free surface, within the cell.

References

- Al-Rashed M, Wjck J, Plewik R, Synowicz P, Ku A. Multiphase CFD modeling: fluid dynamics aspects in scale-up of a fluidized-bed crystallizer. *Chem Eng Process Process Intensif* 2013;63:7–15.
- Avic A, Can M, Etemolu AB. A theoretical approach to the drying process of thin film layers. *Appl Therm Eng* 2001;21(4):465–79.
- Baker A, Bradley C. Modern stalagmite δ^{18} : instrumental calibration and forward modelling. *Global Planet Change* 2010;71(3–4):201–6.
- Bird R, Stewart W, Lightfoot E. *Transport Phenomena*. Wiley International Edition Wiley; 1960.
- Bohacek J. Surface tension model for high viscosity ratios implemented in VOF model. In: ILASS, 23rd annual conference on liquid atomization and spray systems; 2010.
- Burrows C, Phillips C, Milliken A. The thermal oxide reprocessing plant at Sellafield – lessons learned from 10 years of hot operations and their applicability to the DOE environmental management program. In: Wm'06 conference; 2006.
- Chen C, Tsai Y, Lan C. Adaptive phase field simulation of dendritic crystal growth in a forced flow: 2D vs 3D morphologies. *Int J Heat Mass Transfer* 2009;52(5–6):1158–66.
- Cheng J, Yang C, Mao Z-S. CFD-PBE simulation of premixed continuous precipitation incorporating nucleation, growth and aggregation in a stirred tank with multi-class method. *Chem Eng Sci* 2012;68(1):469–80.
- Cui X, Li X, Sui H, Li H. Computational fluid dynamics simulations of direct contact heat and mass transfer of a multicomponent two-phase film flow in an inclined channel at sub-atmospheric pressure. *Int J Heat Mass Transfer* 2012;55(21–22):5808–18.
- Falola A, Borissova A. Crystalsim: a software environment for modelling industrial batch cooling crystallization. *Comput Chem Eng* 2012;38:35–43.
- Graber TA, Taboada ME, Alvarez MN, Schmidt EH. Determination of mass transfer coefficients for crystal growth of nitrate salts. *Cryst Res Technol* 1999;34(10):1269–77.
- Hardt S, Wondra F. Evaporation model for interfacial flows based on a continuum-field representation of the source terms. *J Comput Phys* 2008;227(11):5871–95.
- Haroun Y, Legendre D, Raynal L. Volume of fluid method for interfacial reactive mass transfer: application to stable liquid film. *Chem Eng Sci* 2010;65(10):2896–909.
- Health and Safety Executive. Report of the investigation into the leak of dissolver product liquor at the thermal oxide reprocessing plant (THORP), Sellafield, notified to HSE on 20 April 2005; 2007.
- Heath A, Livk I. Coupled population balance and CFD model for a continuous gibbsite crystalliser. In: Fifth international conference on CFD in the process industries. Melbourne, Australia: CSIRO; 2006.
- Hirt C, Nichols B. Volume of fluid (VOF) method for the dynamics of free boundaries. *J Comput Phys* 1981;39(1):201–25.
- Hu B, Kieweg SL. The effect of surface tension on the gravity-driven thin film flow of Newtonian and power-law fluids. *Comput Fluids* 2012;64:83–90.
- Issa RI. Solution of the implicitly discretised fluid flow equations by operator-splitting. *J Comput Phys* 1986;62:40–65.
- Jun S, Puri VM. 3D milk-fouling model of plate heat exchangers using computational fluid dynamics. *Int J Dairy Technol* 2005;58(4):214–24.
- Kaufmann G. Stalagmite growth and palaeo-climate: the numerical perspective. *Earth Planet Sci Lett* 2003;214:251–66.
- Kaufmann G, Dreybrodt W. Stalagmite growth and palaeo-climate: an inverse approach. *Earth Planet Sci Lett* 2004;224:529–45.
- Li X, Glimm J, Jiao X, Peyser C, Zhao Y. Study of crystal growth and solute precipitation through front tracking method. *Acta Math Sci* 2010;30(2):377–90.
- Mayer M, Bucko J, Benzinger W, Dittmeyer R, Augustin W, Scholl S. Crystallization fouling in experimental micro heat exchangers: optical and thermal investigations. *Exp Heat Trans* 2013;26(5):487–502.
- Mullin J. *Crystallization*. Chemical, petrochemical & process. Elsevier Science; 2001.
- Muzafferija S, Peric M, Sames P, Schellin T. A two-fluid Navier–Stokes solver to simulate water entry. In: Twenty-second symposium on naval hydrodynamics; 1999. p. 277–89.
- Oosterhof H. The growth of sodium nitrate from mixtures of water and isopropoxyethanol. *J Cryst Growth* 1999;198:754–9.
- Phillips C. The thermal oxide reprocessing plant at Sellafield: four years of successful treatment of irradiated nuclear fuel. In: Wm99 conference; 1999.
- Radu A, Bergwerff L, van Loosdrecht M, Picioreanu C. A two-dimensional mechanistic model for scaling in spiral wound membrane systems. *Chem Eng J* 2014;241:77–91.
- Ranjan R, Murthy JY, Garimella SV. A microscale model for thin-film evaporation in capillary wick structures. *Int J Heat Mass Transfer* 2011;54(1–3):169–79.
- Robey HF. Numerical simulation of the hydrodynamics and mass transfer in the large scale, rapid growth of KDP crystals-2: computation of the mass transfer. *J Cryst Growth* 2003;259:388–403.
- Robey HF, Maynes D. Numerical simulation of the hydrodynamics and mass transfer in the large scale, rapid growth of KDP crystals. Part 1: Computation of the transient, three-dimensional flow field. *J Cryst Growth* 2001;222:263–78.
- Romanov D, Kaufmann G, Dreybrodt W. Modeling stalagmite growth by first principles of chemistry and physics of calcite precipitation. *Geochim Cosmochim Acta* 2008;72(2):423–37.
- Sazhin SS. Advanced models of fuel droplet heating and evaporation. *Prog Energy Combust Sci* 2006;32(2):162–214.
- Short MB, Baygents JC, Beck JW, Stone DA, Toomey RS, Goldstein RE. Stalactite growth as a free-boundary problem: a geometric law and its platonic ideal. *Phys Rev Lett* 2005a;94:018501.
- Short MB, Baygents JC, Goldstein RE. Stalactite growth as a free-boundary problem. *Phys Fluids* 2005b;17(8):083101.
- Sultan E, Boundaoud A, Amar MB. Evaporation of a thin film: diffusion of the vapour and Marangoni instabilities. *J Fluid Mech* 2005;543:183–202.
- Walker PG, Sheikholeslami R. Development and validation of an unsteady state numerical model of fouling within a crystalline system. *Dev Chem Eng Mineral Process* 2006;14(1–2):287–302.
- Weber R, Mancini M, Schaffel-Mancini N, Kupka T. On predicting the ash behaviour using computational fluid dynamics. *Fuel Process Technol* 2013;105:113–28.
- Xu T, Pruess K. Solubility and crystal growth of sodium nitrate from mixed alcohol water solvents. Technical report. Curtin University of Technology; 2009.
- Xu Z, Meakin P. Phase-field modeling of solute precipitation and dissolution. *J Chem Phys* 2008;129(1):014705.
- Yeh HS, Wills GB. Diffusion coefficient of sodium nitrate in aqueous solution at 25 deg. as a function of concentration from 0.1 to 1.0 m. *J Chem Eng Data* 1970;15(1):187–9.
- Ying W, Qunhui L, Yangyan Z, Biao Y, Hanzhong T. A CFD-based analysis on trends of heat exchanger fouling. In: Power and Energy Engineering Conference (APPEEC), Asia-Pacific; 2012. p. 1–4.